

# Demonstration of Hopf-link semimetal bands with superconducting circuits

Xinsheng Tan,<sup>1</sup> Mengmeng Li,<sup>1</sup> Danyu Li,<sup>1</sup> Kunzhe Dai,<sup>1</sup> Haifeng Yu,<sup>1,\*</sup> and Yang Yu<sup>1,†</sup>

<sup>1</sup>*National Laboratory of Solid State Microstructures,  
School of Physics, Nanjing University, Nanjing 210093, China*

Hopf-link semimetals exhibit exotic gapless band structures with fascinating topological properties, which have never been observed in nature. Here we demonstrate nodal lines with topological form of Hopf-link chains in artificial semimetal-bands. Driving superconducting quantum circuits with elaborately designed microwave fields, we mapped the momentum space of a lattice to a parameter space of the Hamiltonian for a Hopf-link semimetal. By measuring the energy spectrum, we directly imaged nodal lines in cubic lattices. By tuning the driving fields, we adjusted various parameters of Hamiltonian. Important topological features, such as link-unlink topological transitions and the robustness of the Hopf-link chain structure were investigated. Moreover, we extracted the linking number by detecting the Berry phase associated with different loops encircling nodal lines. This topological invariant clearly reveals the nontrivial topology of the Hopf-link semimetal. Our results provide knowledge for developing new materials and quantum devices.

## Introduction

Topology plays a very important role in physics research, inspiring many findings in condensed matter physics during the past decades. For instance, topological insulators and superconductors [1, 2], which have gapped bulks with topological structures, have been both theoretically and experimentally discovered recently [3–5]. Their physical properties are characterized by nontrivial topological invariants. In addition to protected gapped systems, gapless band structures can also be topological materials, such as Weyl semimetals [6–10]. The study of band-touching manifolds, including semimetals with 0D nodal points (or Dirac points) and 1D nodal lines, deepens our understanding of condensed matter physics [11–16]. Comparing to 0D gapless modes, nodal lines provide richer topological structures: nodal rings can touch at special points, resulting in various shapes of nodal chains. Recently, it was theoretically predicted that semimetals with a unique Hopf-link structure are possible [17, 20]. The Hopf-link, which consists of two rings that pass through the center of each other, represents the simplest topologically nontrivial link. A typical Hamiltonian based on a cubic lattice with Hopf-link structure [17] is given by

$$\begin{aligned} H(\mathbf{k}) &= f_1(\mathbf{k})\sigma_1 + f_2(\mathbf{k})\sigma_3, \\ f_1(\mathbf{k}) &= \sin k_y \cos k_z - \sin k_x \sin k_z, \\ f_2(\mathbf{k}) &= 2 \cos k_x + 2 \cos k_y + \chi, \end{aligned} \quad (1)$$

where  $\sigma_{1,2,3}$  are the Pauli matrices and  $\chi$  is a tunable parameter. Nodal lines in the Brillouin zone can be interpreted as the intersecting lines of two surfaces  $S_x$ :  $f_1(\mathbf{k}) = 0$  and  $S_y$ :  $f_2(\mathbf{k}) = 0$ , forming a novel double-helix structure. Furthermore, due to the periodicity of the Brillouin zone, the cylinder  $S_y$  folds into a torus, so the double-helix structure deforms into a Hopf-chain [as shown in Fig. 1(a)]. The nodal loop cannot shrink to a point without crossing each other, leading to a finite linking number of the Hopf-chain. This basic topolog-

ical invariance can be extracted from the Berry phase [18] carried by a closed loop which encircles the nodal rings [17, 19]. It is easy to verify that Hamiltonians with Hopf-chain structure obey  $PT$  combined symmetry, while breaking the individual  $T$  and  $P$  symmetry since  $[H(\mathbf{k}), PT] = 0$ , where  $T$  is the time-reversal operator and  $P$  is the spatial-inversion operator.

In this paper, we have experimentally realized the topological Hopf-link semimetal bands in a square-lattice, via an analogy between the momentum space with a controllable parameter space in superconducting quantum circuits. By measuring the whole energy spectrum of our system in Brillouin zone, we have clearly imaged the gapless band structure of topological semimetals with linked nodal lines. The topological link-unlink phase transitions in semimetal bands can be manipulated by intentionally adding an extra term in the simulated effective Hamiltonian [17]. Furthermore, to demonstrate the topological robustness of the Hopf-link, a perturbation which breaks  $P$  and  $T$  symmetry, while preserves joint  $PT$  symmetry, is applied. It is verified experimentally that the Hopf-chain of the topological semimetal bands are still present under such perturbations, although the position of nodal lines are changed drastically. To characterize the topological properties of the Hopf-chain, we extracted the linking numbers of nodal lines by detecting the Berry phase after evolving the system along designed paths enclosing or disclosing nodal lines respectively [17, 20]. All of these observations illustrate convincingly the topological properties of Hopf-link semimetals, making these systems promising to develop new materials and devices.

## Results

The superconducting quantum circuits used in our experiment consist of a superconducting transmon qubit embedded in a 3D aluminium cavity [21–25]. The trans-

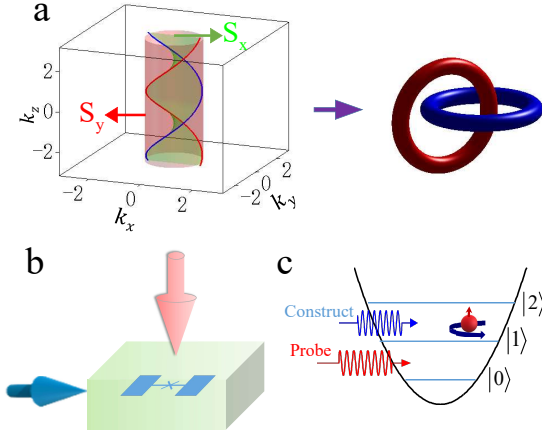


FIG. 1: (Color online) **a**, Nodal lines with a double-helix structure formed by the intersection of two surface  $S_1$  and  $S_2$ . It is topologically equivalent to a Hopf-link. **b**, A superconducting transmon embedded in three-dimensional cavity are driven by designed microwaves, realizing the effective Hamiltonian to simulate Hopf-link semimetals. **c**, The schematic energy structure of a transmon. The lowest three energy levels are used to do the simulation.

mon qubit, composed of a single Josephson junction and two pads ( $250 \mu\text{m} \times 500 \mu\text{m}$ ), is patterned using standard e-beam lithography, followed by double-angle evaporation of aluminium on a  $500 \mu\text{m}$  thick silicon substrate. The thicknesses of the Al film are 30nm and 80nm, respectively. The chip is diced into  $3 \text{ mm} \times 6.8 \text{ mm}$  size to fit into the 3D rectangular aluminium cavity with a TE101 mode resonance frequency of 9.053 GHz. The whole sample package is cooled in a dilution refrigerator to a base temperature 10 mK. The transmon can be considered as an artificial atom located in a cavity and the dynamics of the system is generally described by the theory of circuit QED [26–29]. We designed the energy level of the transmon qubit to let the system work in the dispersive region [27]. The quantum states of the transmon qubit can be controlled by microwaves. IQ mixers combined with 1 GHz arbitrary wave generator (AWG) are used to modulate the amplitude, frequency, and phase of microwave pulses. To readout qubit states, we used an ordinary microwave heterodyne setup. The output microwave is pre-amplified by a HEMT at the 4 K stage in the dilution refrigerator and further amplified by two low-noise amplifiers at room temperature. The microwave is then heterodyned into 50 MHz and collected by ADCs. The readout is performed with a “high power readout” scheme [30]. We sent in a strong microwave on-resonance with the cavity, the transmitted amplitude of the microwave reflects the state of the transmon due to the non-linearity of the cavity QED system.

According to circuit QED theory, the coupled transmon qubit and cavity exhibit anharmonic multiple energy levels. In our experiments, we used the lowest three

energy levels,  $|0\rangle$ ,  $|1\rangle$ , and  $|2\rangle$ , as shown in Fig. 1c. The two states  $|1\rangle$  and  $|2\rangle$  behave as an artificial spin-1/2 particle, whose three components may be denoted by the three Pauli matrices  $\sigma_{1,2,3}$  which can couple with the microwave fields.  $|0\rangle$  is chosen as an ancillary level to probe the energy spectrum of the simulated system. The transition frequencies between different energy levels are  $\omega_{10}/2\pi = 7.172 \text{ GHz}$ ,  $\omega_{21}/2\pi = 6.831 \text{ GHz}$ , respectively, which are independently determined by saturation spectroscopies. The energy relaxation time of the qubit is  $T_1 \sim 7 \mu\text{s}$ , the dephasing time is  $T_2^* \sim 6 \mu\text{s}$ . When we apply microwave drives along the  $x$ ,  $y$ , and  $z$  directions, the effective Hamiltonian of the qubit in the rotating frame may be written as ( $\hbar = 1$  for simplicity)

$$\hat{H} = \sum_{i=1}^3 \Omega_i \sigma_i / 2, \quad (2)$$

where  $\Omega_1$  ( $\Omega_2$ ) corresponds to the frequency of Rabi oscillations along the  $x$  ( $y$ ) axis on the Bloch sphere, which is continuously adjustable by changing the amplitude and phase of the microwave applied to the system.  $\Omega_3 = \omega_{21} - \omega_m$ , is determined by the detuning between the system energy level spacing  $\omega_{21}$  and microwave frequency  $\omega_m$ . By carefully designing the waveform of the AWG, we can modulate the frequency, amplitude, and phase of the microwave. In our experiment, we first calibrated the parameters  $\Omega_1$ ,  $\Omega_2$ , and  $\Omega_3$  using Rabi oscillations and Ramsey fringes, and then designed the microwave amplitude, frequency and phase to set  $\Omega_1 = \Omega(\sin k_y \cos k_z - \sin k_x \sin k_z)$ ,  $\Omega_2(k_x) = 0$ ,  $\Omega_3(k_y) = \Omega(2 \cos k_x + 2 \cos k_y + \chi)$ , point-by-point in the parameter space, with  $\Omega = 10 \text{ MHz}$  being the energy unit here. By mapping the parameter space of the driving two-level system to the  $\mathbf{k}$ -space of a lattice Hamiltonian system, we have realized Eq. (1) exactly.

It was predicted [17] that  $\chi$  plays a crucial role in the realization of the double-helix nodal lines in topological semimetal. We first examined the transition of the Hopf-link band structure with the change of  $\chi$ . Starting from  $\chi = -3$ , we measured the entire energy spectrum of the system over the first Brillouin zone (BZ). The energy spectrum is measured with a spin injection technique [21]. The system is always initialized in  $|0\rangle$ . For a preset  $(k_x, k_y, k_z) \in [-\pi, \pi) \times [-\pi, \pi) \times [-\pi, \pi)$ , the construct microwave pulse drives the two-level system to obtain the Hamiltonian in Eq. (1). A probe microwave pulse is then sent in. When the frequency of the probe microwave matches the energy spacing between the eigenenergy of the Hamiltonian and  $|0\rangle$ , the system will be excited to the eigenstate. A resonant peak of microwave absorption can then be observed. The frequency of the resonant peak represent the eigenenergy. We then gradually changed  $k_x$ ,  $k_y$ , and  $k_z$ , collecting all the eigenenergies from the resonant peaks of the spectrum. We can extract the band

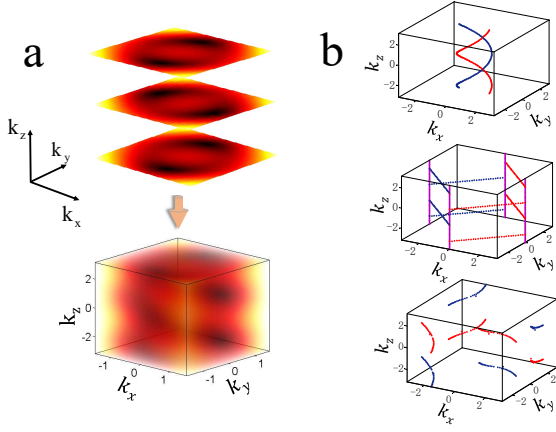


FIG. 2: (Color online) **a**, Measurement of the band structure of the Hopf-link semimetal in the first Brillouin zone. Top panel: Contour plots of the energy gap with varying  $k_z$  gradually in the range of  $[-\pi, \pi]$ . Bottom panel: By collecting all these contour plots together, we obtain the nodal lines of the Hopf-link semimetal. To image the gapless band structure clearly, we set the range of  $(k_x, k_y)$  as  $[-\pi/2, \pi/2] \times [-\pi/2, \pi/2]$ . **b**, Nodal lines obtained from the measured energy spectrum for various  $\chi$ . From top to bottom:  $\chi = -3, 0$ , and  $2$ , respectively.

structure of the semimetal in the first BZ. The zero energy points of the band structure can be directly imaged as nodal points. A chain of connected nodal points forms a nodal line. In Fig. 2b, we plot the nodal lines in the first BZ. A feature of the Hopf-link topological semimetal, which is a double-helix structure, is clearly observed, indicating that we have successfully realized the Hopf-link topological semimetal. In addition, the positions of the nodal lines agree well with the theoretical calculation of Eq. (1) with  $\lambda = -3$ . With increasing  $\chi$ , the surface  $S_2$  expands, leading to a shape change of double-helix. At  $\chi = 0$ ,  $S_2$  touches the boundary of the Brillouin zone, and the double-helix deforms to a cubic-like shape (middle panel in Fig. 2b). At  $\chi = 2$ ,  $S_2$  opens, forming a cylinder centered at  $(\pi, \pi)$ . The intersection of  $S_x$  and  $S_y$  remains a double-helix shape (as shown in the bottom panel of Fig. 2b).

Furthermore, one can take advantage of the full tunability of the superconducting circuit to demonstrate the topological transition and stability. First, we introduce an additional term  $H'_1 = \lambda \sin k_y \sigma_1$  to manipulate the topological link-unlink transition [17]. Here  $H'_1$  is in units of  $\Omega$ , and  $\lambda$  is an adjustable parameter. Shown in Fig. 3a are nodal-line structures for different  $\lambda$ . When  $\lambda < 1$ , two nodal lines are linked. As we increased  $\lambda$  to larger than 1, the two nodal lines become separated, forming two topologically unlinked isolation loops. For  $\lambda = 1$ , the projection of the nodal lines connect at a single point. We can consider this point as the critical point of the transition.

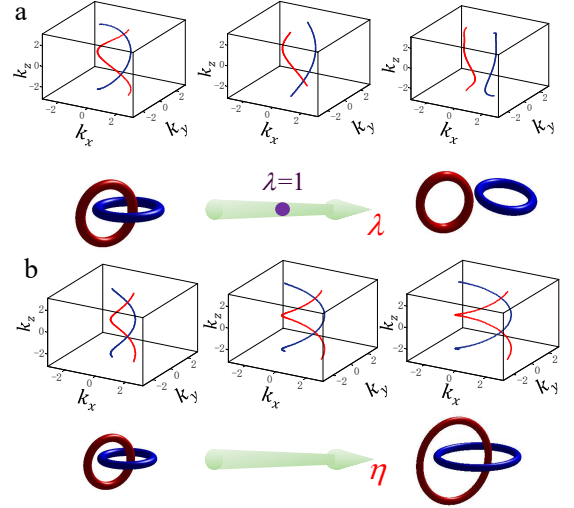


FIG. 3: (Color online) **a**, Link-unlink transition of the Hopf-link semimetal after we added  $H'_1 = \lambda \sin k_y \sigma_1$  to the Hamiltonian in Eq. (1). From left to right: nodal lines with  $\lambda = 0.5, 1$ , and  $1.5$ , respectively. As predicted,  $\lambda = 1$  is the critical point, where two nodal rings only touch at one point. **b**, Stability of the Hopf-link against the perturbation of  $H'_2 = \eta \sigma_3$ . From left to right: nodal lines with  $\eta = -0.5, 0.5$ , and  $1.5$ , respectively.

Since the Hamiltonian in Eq. (1) commutes with  $PT$ , the Hopf-link is protected by the joint space-time symmetry. In order to verify this, we add a term  $H'_2 = \eta \sigma_3$  (with  $\eta$  in units of  $\Omega$ ) to the Hamiltonian in Eq. (1). The modified Hamiltonian violates single  $P$  and  $T$  symmetry but preserves the joint  $PT$  symmetry. It is found that with increasing  $\eta$ , the band structure is distorted dramatically, and the positions as well as neighborhood geometries of the band-crossing lines are changed significantly. Nevertheless, these nodal lines are persistently present in the BZ without opening any gap, thus forming a double-helix, as shown in Fig. 3b. This strongly supports that the Hopf-link structure is protected by the  $PT$  symmetry.

Besides the band structure, the topological invariant quantity is another feature associated with topological phenomena. To characterize the linking number of the Hopf-link, which describes the connection of the nodal lines, we detect the Berry phase carried by a closed path enclosing or disclosing nodal lines in the parameter space from an adiabatic procedure [31, 32]. For the dashed loop showed in Fig. 4a, we design a closed path enclosing the Hopf-link chains in Brillouin zone to probe the Berry phase. The entire adiabatic evolution consists of two parts. One path, marked by the purple dashed line, which threads the link loop, contributes a Berry phase  $\pi$ . The other part, marked with grey dashed lines, contributes a null Berry phase. However, the loop in Fig. 4a is in momentum space. We have to map it from mo-

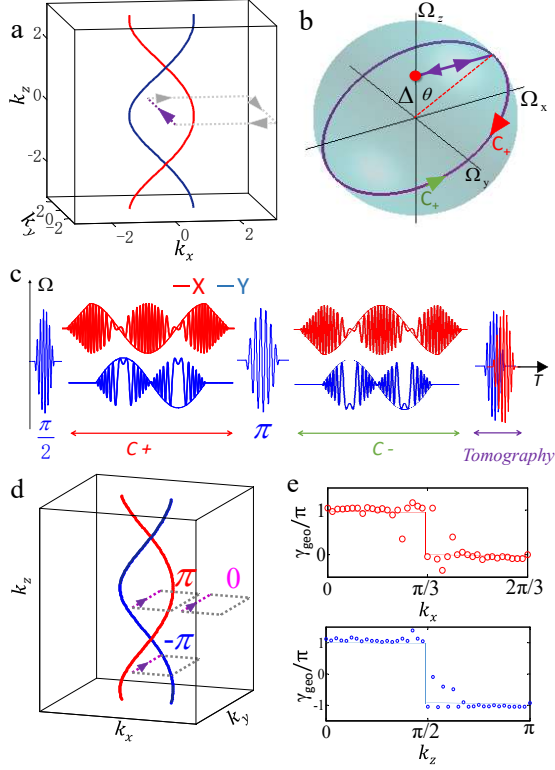


FIG. 4: (Color online) **a**, Schematic of an example of closed path (dashed line) in the first Brillouin zone to accumulate Berry phase, from which the linking number can be characterized. **b**, Evolving path in parameter space of qubit mapped from momentum space in **a**. **c**, Schematic of time profile to probe Berry phase accumulated from the evolution in **b**. **d**, Dependence of the Berry phase carried on the loop of the closed path. There are three typical values:  $\pi$ ,  $-\pi$ , and 0. **e**, Berry phase measured as a function of  $k_x$  (top panel) and  $k_z$  (down panel), respectively.

momentum space to the parameter space of the superconducting qubit, as illustrated in Fig. 4b. Theoretically, the evolution path denoted by the purple dashed line is topologically equivalent to a circle along the meridian of the Bloch sphere. Without loss of generality, we design a geodesic to replace the original path by choosing  $\{\Omega_x, \Omega_y, \Omega_z\} = \{\sin \theta \cos \phi + \Lambda_1, \Lambda_2 \sin \phi, \cos \theta \cos \phi + \Lambda_1\}$ , where  $\theta \in [0, \pi]$  and  $\phi \in [0, 2\pi]$  are spherical coordinates. By tuning the parameters  $\Lambda_1$  and  $\Lambda_2$ , we can implement any closed path in the Brillouin zone. To detect the accumulated Berry phase after time evolution, we used the Ramsey fringe interference technique [33, 34]. This adiabatic approach has been demonstrated to be a convenient method to measure the Berry phase in superconducting circuits. If one prepares the qubit in a superposition state  $(|0\rangle + |1\rangle)/\sqrt{2}$ , the evolution of  $|0\rangle$  and  $|1\rangle$  will acquire a relative Berry phase  $\gamma_{\text{geo}}$ , which equals to 1/2 of the solid-angle enclosed by the circle denoted as  $C_{\pm}$ . The sign depends on the path direction. The relative phase

of the quantum state after the evolution is extracted as  $\Phi_{\text{total}} = \arctan(\sigma_y/\sigma_x)$ , which equals four times of the Berry phase. This agrees with the theoretical prediction, confirming the topological properties of the nodal rings. As shown in Fig. 4d, by adjusting the parameters  $\Lambda_1$  and  $\Lambda_2$ , we can move the position of the closed path in  $\mathbf{k}$ -space. By moving the purple dashed line along the  $k_x$  axis on the  $k_z = 0$  plane, the originally designed closed loop changes from enclosing to disclosing the red nodal line. The geometric phase measured then switches from  $\pi$  to 0 abruptly at  $k_x = \pi/3$ , indicating that the closed path in the qubit parameter space is no longer a geodesic circle at this critical point. Furthermore, by moving the loop along  $k_z$  on the  $k_x = 0$  plane, the closed path changes from enclosing a red nodal line to a blue nodal line. The Berry phase jumps from  $\pi$  to  $-\pi$  at  $k_z = \pi/2$ , corresponding to the Berry phase obtained along the  $C_{\pm}$  loop. Therefore, in the first Brillouin zone, the Berry phase measured are well characterized topological connection of the nodal ring [17].

## Discussion

Experimentally realizing the Hopf-link band structures and thus investigating related interesting topological properties in real condensed matter systems are a challenge. Nodal lines with Hopf-chain structure have not been observed in any multi-particle system so far. The lack of technique for directly imaging the whole momentum-dependent electronic energy spectrum also prohibits the fundamental research of the complex topological band structure, noting only a part of the electronic spectra (or information of Fermi surfaces/points) may be inferred from the angle-resolved photoemission spectroscopy data (or quantum oscillation measurements) in bulk condensed matter systems. Furthermore, it seems extremely difficult to tune the parameters continuously for studying rich topological properties including various topological quantum phase transitions in real materials. Therefore, our simulations using artificial quantum systems, like superconducting quantum circuits, provide faithful topological properties of the system, which are useful to design related materials and devices.

## Methods

We used the Ramsey fringe interference technique to measure the Berry phase. The schematic time profile of the measurement procedure is shown in Fig. 4c. At first, the qubit is initialized at  $(|0\rangle + |1\rangle)/\sqrt{2}$  by a  $\pi_y/2$  pulse. Then, we ramp the Hamiltonian linearly from  $\{0, 0, \Omega_z\}$  to  $\{\Omega_x, 0, \Omega_z\}$ , followed by a traverse along the geodesic path  $C_+$ , by ramping the parameter  $\phi = 2\pi t/T_{\text{ramp}}$ , where  $T_{\text{ramp}} = 400$  ns. Since  $\Omega$  is set as  $2\pi \times 25$  MHz,

the adiabaticity in the evolution is satisfied. Instantaneous spin-up and spin-down eigen-states of Hamiltonian (denoted by  $|\uparrow\rangle$  and  $|\downarrow\rangle$ ) obtains the relative phases  $\Phi_{c\pm} = \pm\gamma_{\text{geo}} + \phi_{\text{dym}\uparrow(\downarrow)}$  respectively, where the Berry phase  $\gamma_{\text{geo}} = \pi$  in our experiments, and  $\phi_{\text{dym}\uparrow(\downarrow)}$  is the dynamical phase obtained in the procedure. After a resonant spin-echo  $\pi$  pulse is applied, the system evolves along  $C_-$ , which has an opposite direction to  $C_+$ , acquiring  $\Phi_{c\mp} = \mp\gamma_{\text{geo}} + \phi_{\text{dym}\downarrow(\uparrow)}$ . The states finally evolve to  $\exp[i(\phi_{\text{dym}\uparrow} + \phi_{\text{dym}\downarrow} + 2\gamma_{\text{geo}})]|\uparrow\rangle$  and  $\exp[i(\phi_{\text{dym}\uparrow} + \phi_{\text{dym}\downarrow} - 2\gamma_{\text{geo}})]|\downarrow\rangle$ , therefore, the net relative phase gained during the complete procedure equals  $4\gamma_{\text{geo}}$  [33]. At the end of the evolution, we extract the phase of the qubit state by quantum state tomography. To map different paths in the first Brillouin zone,  $\Lambda_1$  and  $\Lambda_2$  are designed at various values. For instance, to move the closed loop with fixed  $k_z = 0$  as shown in Fig. 4d,  $\Lambda_1$  is varied as  $(2\cos k_x - \lambda)/2$  and  $\Lambda_2$  is set as 1.

---

\* Electronic address: hfyu@nju.edu.cn

† Electronic address: yuyang@nju.edu.cn

- [1] M. Z. Hasan, C. L. Kane, Colloquium: Topological insulators. *Rev. Mod. Phys.* **82**, 3045–3067 (2010).
- [2] X.-L. Qi, S.-C. Zhang, Topological insulators and superconductors. *Rev. Mod. Phys.* **83**, 1057–1110 (2011).
- [3] X. Wan, A. M. Turner, A. Vishwanath, S. Y. Savrasov, Topological semimetal and Fermi-arc surface states in the electronic structure of pyrochlore iridates. *Phys. Rev. B* **83**, 205101 (2011).
- [4] M. König, S. Wiedmann, C. Brune, A. Roth, H. Buhmann, L. W. Molenkamp, X. Qi, S. Zhang, Quantum spin Hall insulator state in HgTe quantum wells. *Science* **318**, 766–770 (2007).
- [5] C. L. Kane, E. J. Mele,  $Z_2$  topological order and the quantum spin Hall effect. *Phys. Rev. Lett.* **95**, 146802 (2005).
- [6] L. Lu, Z. Wang, D. Ye, L. Ran, L. Fu, J. D. Joannopoulos, M. Soljačić, Experimental observation of Weyl points. *Science* **349**, 622–624 (2015).
- [7] S.-Y. Xu, I. Belopolski, N. Alidoust, M. Neupane, G. Bian, C. Zhang, R. Sankar, G. Chang, Z. Yuan, C.-C. Lee, S.-M. Huang, H. Zheng, J. Ma, D. S. Sanchez, B. Wang, A. Bansil, F. Chou, P. P. Shibayev, H. Lin, S. Jia, M. Z. Hasan, Discovery of a Weyl fermion semimetal and topological Fermi arcs. *Science* **349**, 613–617 (2015).
- [8] Z. Liu, J. Jiang, B. Zhou, Z. Wang, Y. Zhang, H. Weng, D. Prabhakaran, S. Mo, H. Peng, P. Dudin, A stable three-dimensional topological Dirac semimetal  $\text{Cd}_3\text{As}_2$ . *Nature materials* **13**, 677–681 (2014).
- [9] B. Q. Lv, H. M. Weng, B. B. Fu, X. P. Wang, H. Miao, J. Ma, P. Richard, X. C. Huang, L. X. Zhao, G. F. Chen, Z. Fang, X. Dai, T. Qian, H. Ding, Experimental discovery of Weyl semimetal TaAs. *Phys. Rev. X* **5**, 031013 (2015).
- [10] G. Bian, T. Chang, R. Sankar, S. Xu, H. Zheng, T. Neupert, C. Chiu, S. Huang, G. Chang, I. Belopolski, *et al.*, Topological nodal-line fermions in spin-orbit metal  $\text{PbTaSe}_2$ . *Nat. Commun.* **7**, 10556–10556 (2016).
- [11] O. Vafek, A. Vishwanath, Dirac fermions in solids: From high-Tc cuprates and graphene to topological insulators and Weyl semimetals. *Annual Review of Condensed Matter Physics* **5**, 83–112 (2014).
- [12] R. Yu, H. Weng, Z. Fang, X. Dai, X. Hu, Topological node-line semimetal and dirac semimetal state in antiperovskite  $\text{Cu}_3\text{PdN}$ . *Phys. Rev. Lett.* **115**, 036807 (2015).
- [13] Y. Kim, B. J. Wieder, C. L. Kane, A. M. Rappe, Dirac line nodes in inversion-symmetric crystals. *Phys. Rev. Lett.* **115**, 036806 (2015).
- [14] A. Burkov, M. D. Hook, L. Balents, Topological nodal semimetals. *Physical Review B* **84** (2011).
- [15] J. E. Moore, Y. Ran, X. Wen, Topological surface states in three-dimensional magnetic insulators. *Phys. Rev. Lett.* **101**, 186805 (2008).
- [16] M. Neupane, S.-Y. Xu, R. Sankar, N. Alidoust, G. Bian, C. Liu, I. Belopolski, T.-R. Chang, H.-T. Jeng, H. Lin, A. Bansil, F. Chou, M. Z. Hasan, Observation of a three-dimensional topological Dirac semimetal phase in high-mobility  $\text{Cd}_3\text{As}_2$ . *Nat. Commun.* **5**, 3786 (2014).
- [17] W. Chen, H.-Z. Lu, J.-M. Hou, Topological semimetals with a double-helix nodal link. *Phys. Rev. B* **96**, 041102 (2017).
- [18] M. V. Berry, Quantal phase factors accompanying adiabatic changes. *Proceedings of The Royal Society of London* **392**, 45–57 (1984).
- [19] P.-Y. Chang, C.-H. Yee, Weyl-link semimetals. *Phys. Rev. B* **96**, 081114 (2017).
- [20] Z. Yan, R. Bi, H. Shen, L. Lu, S.-C. Zhang, Z. Wang, Nodal-link semimetals. *Phys. Rev. B* **96**, 041103 (2017).
- [21] X. Tan, Y. Zhao, Q. Liu, G. Xue, H. Yu, Z. D. Wang, Y. Yu, Realizing and manipulating space-time inversion symmetric topological semimetal bands with superconducting quantum circuits. *npj Quantum Materials* **2**, 60 (2017).
- [22] H. Paik, D. I. Schuster, L. S. Bishop, G. Kirchmair, G. Catelani, A. P. Sears, B. R. Johnson, M. J. Reagor, L. Frunzio, L. I. Glazman, S. M. Girvin, M. H. Devoret, R. J. Schoelkopf, Observation of high coherence in Josephson junction qubits measured in a three-dimensional circuit QED architecture. *Phys. Rev. Lett.* **107**, 240501 (2011).
- [23] I. Buluta, F. Nori, Quantum Simulators. *Science* **326**, 108–111 (2009).
- [24] K. W. Murch, S. J. Weber, C. Macklin, and I. Siddiqi, Observing single quantum trajectories of a superconducting quantum bit. *Nature* **502**, 211 (2013).
- [25] Z. Kim, B. Suri, V. Zaretsky, S. Novikov, K. D. Osborn, A. Mizel, F. C. Wellstood, and B. S. Palmer, Decoupling a Cooper-pair box to enhance the lifetime to 0.2 ms. *Phys. Rev. Lett.* **106**, 120501 (2011).
- [26] X. Gu, A.F. Kockum, A. Miranowicz, Y.X. Liu, F. Nori, Microwave photonics with superconducting quantum circuits. *Physics Reports* **718-719**, 1–102 (2017).
- [27] J. Q. You, F. Nori, Quantum information processing with superconducting qubits in a microwave field. *Phys. Rev. B* **68**, 064509 (2003).
- [28] A. Wallraff, D. I. Schuster, A. Blais, L. Frunzio, R. Huang, J. Majer, S. Kumar, S. M. Girvin, R. J. Schoelkopf, Strong coupling of a single photon to a superconducting qubit using circuit quantum electrodynamics. *Nature* **431**, 162 (2004).
- [29] J. Q. You, F. Nori, Atomic physics and quantum optics

- using superconducting circuits. *Nature* **474**, 589 (2011).
- [30] M. D. Reed, L. DiCarlo, B. R. Johnson, L. Sun, D. I. Schuster, L. Frunzio, R. J. Schoelkopf, High-fidelity read-out in circuit quantum electrodynamics using the Jaynes-Cummings nonlinearity. *Phys. Rev. Lett.* **105**, 173601 (2010).
  - [31] D. A. Abanin, T. Kitagawa, I. Bloch, E. Demler, Interferometric approach to measuring band topology in 2D optical lattices. *Phys. Rev. Lett.* **110**, 165304 (2013).
  - [32] D. Xiao, M. Chang, Q. Niu, Berry phase effects on electronic properties. *Rev. Mod. Phys.* **82**, 1959–2007 (2010).
  - [33] P. J. Leek, J. M. Fink, A. Blais, R. Bianchetti, M. Göppl, J. M. Gambetta, D. I. Schuster, L. Frunzio, R. J. Schoelkopf, A. Wallraff, Observation of Berry’s phase in a solid-state qubit. *Science* **318**, 1889–1892 (2007).
  - [34] X. Tan, D.-W. Zhang, Z. Zhang, Y. Yu, S. Han, S.-L. Zhu, Demonstration of geometric Landau-Zener interferometry in a superconducting qubit. *Phys. Rev. Lett.* **112**, 027001 (2014).

#### Acknowledgements:

We would like to thank H. Zhang for helpful suggestion, discussion, and proof reading of the manuscript. We also thank F. Nori for giving many helpful comments and suggestions after proof reading of the manuscript. This work was partly supported by the the NKRD of China (Grant No. 2016YFA0301802), NSFC (Grant No. 11274156, No. 11504165, No. 11474152, No. 61521001)